Tellus
SERIES A
DYNAMIC
METEOROLOGY
AND OCEANOGRAPHY
PUBLISHED BY THE INTERNATIONAL METEOROLOGICAL INSTITUTE IN STOCKHOLM

Tellus (2008), 60A, 789–802
Printed in Singapore.
TELLUS

A numerical study of ice-drift divergence by cyclonic wind with a Lagrangian ice model

By YUSUKE KAWAGUCHI[1,2]* and HUMIO MITSUDERA[2], [1]*Graduate School of Environmental Earth Science, Hokkaido University, Sapporo 060-0810, Japan;* [2]*Institute of Low Temperature Science, Hokkaido University, Sapporo 060-0819, Japan*

(Manuscript received 1 March 2007; in final form 2 January 2008)

ABSTRACT

In polar regions low-pressure systems drive sea ice divergence, which can accelerate summer sea ice melt through energy absorption at resulting open water areas. This paper examines the mechanisms that cause the ice divergence and its seasonal change with a Lagrangian ice model. We focus on the effects of initial ice concentration, ice strength and ocean stratification. A series of idealized simulations (initially at 5 km resolution) are carried out with a Rankine combined vortex as external wind forcing. We have found a characteristic length scale r_1^* in free drift, based on the influence of the Coriolis term. The results show that ice concentration decreases most greatly within the range of r_1^*. In addition, ice divergence becomes small in the inner region for high concentrations (i.e. over 0.95), due to inward internal force blocking divergent deformations. The effects of ocean stratification on ice-drift divergence are also examined. Numerical results show that as the density stratification increases divergent Ekman flows beneath ice further promote the ice-drift divergence and lead to more reduction in the ice concentration through thinning of surface Ekman layer.

1. Introduction

Various recent studies have indicated significant decrease in sea-ice extent and area in the Arctic (e.g. Johannessen et al., 1995; Maslanik et al., 1996; Cavalieri et al., 1997; Serreze et al., 2003; Comiso, 2006; Nghiem et al., 2007; Stroeve et al., 2007). Serreze et al. (2003) concluded that the ice area and extent in September 2002 were remarkably small and that this is a consequence of persistent low pressure and high temperature over the Arctic Ocean in the summer of 2002, which promoted ice drift divergence due to cyclonic winds and caused a rapid melt. In general, open water areas absorb much more solar radiation than the ice covered surface, and this heat is then utilized for ice melting. The ice melt generates more open water and further ice melt and gives rise to a positive ice-albedo feedback (e.g. Maykut and Perovich, 1987; Ohshima and Nihashi, 2005). Therefore, the open water formation by a persistent low-pressure system can be considered as a trigger of the ice cover reduction over the Arctic Ocean during summer.

The response of sea ice to surface winds varies greatly with seasons. Thorndike and Colony (1982) demonstrated that the sea ice speed and rotation angle from geostrophic winds are generally larger in summer than those in fall, winter, and spring. They argued on the smaller winter values in terms of an atmospheric boundary layer and larger internal stress than those of summer. Furthermore, Serreze et al. (1989) examined in detail the seasonality of the rotation angle of the ice motion from the geostrophic winds, considering it as an index of ice divergence, and diagnosed it under low-pressure systems successfully. They found that ice divergence under low-pressure systems is greater in summer than those of other seasons.

There are very few investigations dealing directly with dynamics of sea-ice drift under low pressure systems, and hence, basic questions still remain. The following are a few examples. In a free drift case, Thorndike and Colony (1982) suggested that ice drift angle to geostrophic winds (and hence divergence) is large where winds are sufficiently small. This implies that ice divergence is large near the centre of the cyclone. When the sea ice concentration (SIC) is large, however, Haapala et al. (2005) demonstrated in a series of numerical experiments that the sea ice does not diverge near the centre of the cyclone if the ice–water and ice–air turning angles are the same. This suggests that internal stress must be important for cases with large SIC. Although this is intuitively reasonable, we do not yet know how the internal stress works to prevent sea ice from divergence. Another question is how the near surface stratification affects the ice–water stress turning angle. The ice divergence/convergence depends greatly on the turning angle (e.g. Haapala et al., 2005). However, what causes the changes in the turning angle is not yet clear. In polar oceans, near-surface stratification varies with

*Corresponding author.
e-mail: kawa-y@lowtem.hokudai.ac.jp
DOI: 10.1111/j.1600-0870.2008.00321.x

season greatly (e.g. Rudels et al., 1996, 1991; Steel and Boyd, 1998). This may affect the ice divergence through the changes in ice–water turning angle, besides the ice interaction processes.

Considering the arguments above, there are three issues of interest in this study. First, we revisit a free-drift case, paying attention to ice divergence characteristics under a stationary cyclone. We specify non-dimensional parameters, which represent relative importance of terms in the momentum equations. Second, we investigate the effects of ice internal stress as to how it modifies sea ice drift as SIC varies. For these two issues, we conducted numerical experiments using a Lagrangian ice model, and discuss the results in conjunction with analytical solutions. We believe it is important to understand ice dynamics under a stationary cyclone as a basis for exploring more realistic cases, such as those with moving cyclones. Further, the persistent low pressure during summer in the Arctic region promoted a recent decrease of sea-ice extent (Serreze et al., 2003), which is also a motivation to deal with stationary cyclones in this study.

We adopt the Smoothed Particle Hydrodynamics (hereafter SPH) algorithm to perform experiments of ice response to winds. SPH represents the characteristic ice behaviour, which retains its properties for long periods of time, and reduces numerical diffusion by distributing particles densely where the gradient of a certain property is large (e.g. Gutfraind and Savage, 1997; Lindsay and Stern, 2004). Recently, Lindsay and Stern (2004) applied a Lagrangian model with the SPH method to a simulation of the Arctic Ocean, and successfully reproduced observed buoy motions.

Our third interest concerns the effects of stratification in the ocean surface layer on the ice divergence. In order to pursue this issue, the Lagrangian ice model is coupled to the Princeton Ocean Model (POM) that incorporates a turbulent closure model for the surface layer. Hence, the surface Ekman layer is calculated directly, and so no turning angle is presumed for the formulation of ice–water stresses.

This paper is organized as follows. In Section 2, the Lagrangian ice model and the ice–ocean coupled model are described. In Section 3, sensitivity of the ice-drift divergence to wind forcing, initial SIC and ice strength is numerically examined by using the Lagrangian ice model. Additionally, analytic solutions are obtained to understand the role of each term in the momentum balance. The role of the oceanic stratification on ice motion is discussed in Section 4. The results are then summarized in Section 5.

2. Model

2.1. Lagrangian sea ice model

2.1.1. Governing equations. In the model, all equations are integrated in a Lagrangian manner. That is, each ice parcel can individually move by maintaining its own properties, such as SIC and ice thickness. The model is based on a momentum equation with ice interaction and conservation equations, which include equations of mean ice thickness, ice concentration and area of a particle.

The momentum equation can be expressed as

$$\rho h \frac{\mathrm{d}\mathbf{u}}{\mathrm{d}t} + \rho h f \mathbf{k} \times \mathbf{u} = \tau_{\mathrm{a}} + \tau_{\mathrm{w}} + \nabla \cdot \sigma - \rho h g \nabla \eta, \tag{1}$$

where $\mathbf{u} = (u,v)$ is the ice velocity vector, ρ the ice density, h the mean thickness of ice, f the Coriolis parameter, g gravity, η the surface elevation and σ is the internal stress tensor of sea ice. Sea ice motion is determined by five forces, namely air–ice stress, water-ice stress, Coriolis force, internal force, and sea surface tilting. In this study, the response of ice to winds is considered only on a short time scale, in which effects of thermodynamic processes can be ignored. In the Lagrangian point of view, the equations are solved at the position of each arbitrarily moving particle, and advective terms need not be evaluated separately.

The air–ice and water–ice stresses are determined by the bulk formulae

$$\tau_{\mathrm{a}} = \rho_{\mathrm{a}} C_{\mathrm{a}} |\mathbf{U}_{\mathrm{a}}| (\cos\theta_{\mathrm{a}} + \sin\theta_{\mathrm{a}} \mathbf{k}\times) \mathbf{U}_{\mathrm{a}}, \tag{2}$$

$$\tau_{\mathrm{w}} = -\rho_{\mathrm{w}} C_{\mathrm{w}} |\mathbf{u}| (\cos\theta_{\mathrm{w}} + \sin\theta_{\mathrm{w}} \mathbf{k}\times) \mathbf{u}, \tag{3}$$

where $\mathbf{U}_{\mathrm{a}}$ is geostrophic wind, ρ_{a} and ρ_{w} are the air and water density, C_{a} and C_{w} are the air and water drag coefficients, and θ_{a} and θ_{w} are turning angles for air stress and water stress, respectively. In τ_{w}, the effect of geostrophic current is neglected for the ice-only model. This formula will be used in Section 3.

The geostrophic wind has the form of a stationary Rankine combined vortex (Fig. 1), of which magnitude is given by

$$U_{\mathrm{a}} = \begin{cases} \omega r & r < R \\ \omega R^2/r & r \geq R, \end{cases} \tag{4}$$

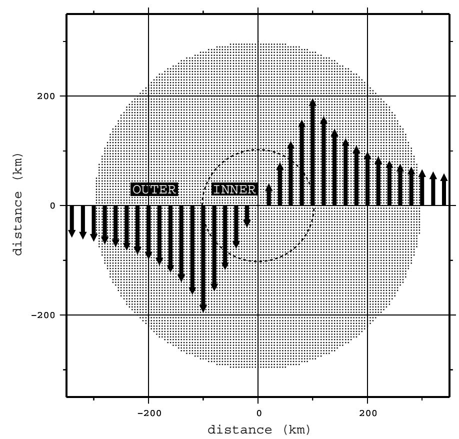

Fig. 1. Model domain and geostrophic wind for the standard case. The model ice configuration has a circular shape with a diameter of 600 km and consists of 16 000 particles uniformly distributed initially by 5 km. The geostrophic wind is a Rankine combined vortex with an inner region of radius 100 km.

where $r = (x^2 + y^2)^{1/2}$ is radial position and ω is angular velocity in the inner region. R is the radius of the vortex core set at $R = 100$ km in this study. We note that this type of wind forcing has an interior with a constant vorticity of 2ω (solid rotation) that generates divergent Ekman transport and strong Ekman pumping, while it has an exterior with zero wind stress curl (irrotational flow). In the inner region ($r < R$), the wind velocity linearly increases with r from the centre and has a maximum at the boundary ($r = R$). In the outer region ($r > R$), the wind velocity inversely decreases with distance and approaches to zero assymptotically.

The Rankine vortex with R=100 km may be a relevant approximation of the velocity field in a polar low. Shapiro et al. (1987) captured the detailed structure of the polar low from meteorological measurements via aircraft. According to them, the centre core was roughly 100 km in radius. Furthermore, it had a remarkably large relative vorticity in the centre core, with a small vorticity on the outside, which is well modeled by the Rankine vortex. The Rankine vortex has also been regarded as a typical of atmospheric vortex, which provides a good fit to a number of cyclones. James (1950) estimated R to be 200–500 km as the radius of the maximum pressure gradient (or geostrophic velocity). He also pointed out its difficulty in practical application to some meteorological analyses, because the Rankine vortex has infinite kinetic energy when integrated for $r \to \infty$. However, since we provide non-dimensional analyses in Sections 3.2 and 3.3, the results are still agreeable even for large-scale cyclones.

In this study, the viscous-plastic rheology of Hibler (1979) is adopted. The internal stress is hence written as (see Leppäranta, 2005)

$$\sigma = \frac{P}{2}\left[\frac{\dot{\varepsilon}_I}{\max(\Delta, \Delta_0)} - 1\right]\mathbf{I} + \frac{P}{2e^2\max(\Delta, \Delta_0)}\dot{\varepsilon}', \qquad (5)$$

where $\dot{\varepsilon}$ denotes a strain rate tensor and $\dot{\varepsilon}' = \dot{\varepsilon} - \frac{1}{2}\mathrm{tr}\dot{\varepsilon}\mathbf{I}$ and $\Delta = (\dot{\varepsilon}_I^2 + \dot{\varepsilon}_{II}^2 e^{-2})^{1/2}$. $\dot{\varepsilon}_I$ and $\dot{\varepsilon}_{II}$ are the strain rate invariants equal to the sum and difference of the principal strain rate components, respectively. Δ_0 is the maximum linear viscous creep rate. e is the ratio of compressive strength to shear strength, or aspect ratio of the yield ellipse of Hibler's rheology (Fig. 2). P is ice strength such that

$$P = P_0 h \exp[-C(1 - A)], \qquad (6)$$

in which C is a strength constant for SIC, h is mean ice thickness, P_0 is an ice strength constant and A is SIC. According to (6), P, and consequently σ, is highly sensitive to SIC through C. The e-folding scale for ice strength corresponds to $A = 0.95$ when $C = 20$. A summary of the parameters for a standard case is shown in Table 1. indent In this study, conservation equations for h, A and area of particle S are mainly based on divergence of sea ice motion, and include no thermodynamical processes, such as decay or growth of ice. Thus, they are written in the

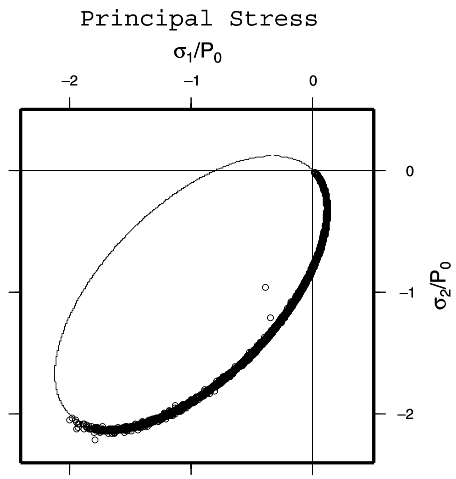

Fig. 2. Normalized principal stress computed in the model along with the elliptic yield curve.

Table 1. Model parameters for the standard case for the ice-only model in Section 3

Parameter	Symbol	Value
Ice density	ρ	910 kg m^{-3}
Air density	ρ_a	1.3 kg m^{-3}
Water density	ρ_w	1000 kg m^{-3}
Wind drag coefficient	C_a	0.0012
Current drag coefficient	C_w	0.0055
Wind stress turning angle	θ_a	30°
Water stress turning angle	θ_w	30°
Ice strength constant	P_0	5000 Pa
Yield ellipse aspect ratio	e	2
Strength constant for compactness	C	20
Maximum creep rate	Δ_0	2.0×10^{-9} s^{-1}
Coriolis parameter	f	1.46×10^{-4} s^{-1}
Radius of Rankine vortex	R	100 km
Angular velocity of geostrophic wind	ω	1.0×10^{-4} s^{-1}
Initial ice thickness	h_0	1.0 m

Lagrangian form as

$$\frac{\mathrm{d}}{\mathrm{d}t}\begin{pmatrix} A \\ h \\ S \end{pmatrix} = \begin{pmatrix} -A \\ -h \\ S \end{pmatrix} \nabla \cdot \mathbf{u}. \qquad (7)$$

The initial values of h and S are $h_0 = 1$ m and $S_0 = 25$ km^2, respectively.

2.1.2. SPH formalism. The SPH formalism determines a local smoothed average field quantity $f(\mathbf{r})$ as a weighted summation of the property at locations of neighbouring particles. The weighted average at position $\mathbf{r}$ is derived from an area integral with a kernel function W, and then

$$\langle f(\mathbf{r})\rangle = \int f(\mathbf{r}')W(|\mathbf{r} - \mathbf{r}'|, \ell)\mathrm{d}s' \qquad (8)$$

where $f(\mathbf{r})$ is a two-dimensional scalar field. W is a kernel function, and ℓ is a smoothing length that determines the accuracy of estimates. This indicates that the intergral representation of the function $f(\mathbf{r})$ is approximated by summing up the values of the nearest neighbouring particles. The SPH integral approximation is, in general, of second order accuracy for ℓ. The continuous SPH representation for $f(\mathbf{r})$ can be rewritten in the following discretized form

$$\langle f(\mathbf{r_i})\rangle = \sum_{k=1}^{N} f_k S_k W_k(|\mathbf{r_i} - \mathbf{r_k}|, \ell), \tag{9}$$

where S_k is the area of particle k, and $|\mathbf{r}_i - \mathbf{r}_k|$ is the distance to the kth particle. N is the number of adjacent particles used to compute the integral. The kernel W must be a radially symmetric function with unit area

$$\int W(|\mathbf{r} - \mathbf{r}'|, \ell)\mathrm{d}\mathbf{r}' = 1. \tag{10}$$

In this study, the Gaussian kernel

$$W(|\mathbf{r} - \mathbf{r}'|, \ell) = \frac{1}{\pi \ell^2} \exp\left(-\frac{|\mathbf{r} - \mathbf{r}'|^2}{\ell^2}\right), \tag{11}$$

is utilized, which is sufficiently stable and accurate even for the disorderd particles.

The particle location changes every time step and the particles are distributed irregurarly in the Lagrangian manner. Therefore, the derivative cannot be determined simply by differencing the properties of adjacent grids. However, we can solve this problem through the key aspect of SPH approximation (e.g. Lindsay and Stern, 2004)

$$\langle \nabla f(\mathbf{r})\rangle = \int f(\mathbf{r}')\nabla W(|\mathbf{r} - \mathbf{r}'|, \ell)\mathrm{d}s' \tag{12}$$

$$\simeq \sum_{k=1}^{N} S_k[f(\mathbf{r}') - f(\mathbf{r})]\nabla_i W(|\mathbf{r_i} - \mathbf{r_k}|, \ell). \tag{13}$$

This means that the SPH integral representation gives an approximated derivative estimate, which does not include the function derivative, but the derivative of the smoothing kernel W.

2.1.3. Neighbouring particles. In principle, the summations in (9) and (13) should include all of the particles in the model because the support domain of the Gaussian function is spatially infinite. In practice, however, the particles more than one or two length scales away from the point of interest have little impact. In order to improve numerical efficiency, the summations are performed only on the nearest 30 particles, which are searched every half day. If an ice field consisting of uniformly distributed particles within a space of smoothing length ℓ, the summation of the Gaussian kernel over a square area of $4\ell \times 4\ell$ would be

$$\sum_{k}^{25} W_k S_k = \sum_{k}^{25} \frac{S_k}{\ell^2 \pi} \exp\left(-\frac{|\mathbf{r}_i - \mathbf{r}_k|^2}{\ell^2}\right) = 0.999928. \tag{14}$$

This shows that the condition of (10) can be sufficiently satisfied if the ℓ is roughly $\sqrt{S_0}$ and 30 particles are used.

Figure 2 shows normalized principal components of the internal stress, that is, σ_1 and σ_2, computed in the model. As it can be seen, the SPH representation provides sufficient accuracy, showing that the relationship between σ_1 and σ_2 corresponds well with the elliptic yield curve.

2.1.4. Predicting scheme. To update velocities, the third-order Runge–Kutta scheme is used as follows:

$$\mathbf{u}_i^{n+1} = \mathbf{u}_i^n + \frac{\Delta t}{6}\left[\left(\frac{\mathrm{d}\mathbf{u}^*}{\mathrm{d}t}\right)_i^n + 4\left(\frac{\mathrm{d}\mathbf{u}^*}{\mathrm{d}t}\right)_i^{n+1/2} + \left(\frac{\mathrm{d}\mathbf{u}^*}{\mathrm{d}t}\right)_i^{n+1}\right], \tag{15}$$

where $\mathbf{u}_i^n$ is the velocity of particle i at step n. Δt is a time step, which is set to be 10 s. $\frac{\mathrm{d}u^*}{\mathrm{d}t}$ is computed every half time step based on (1), and the weighted sum is utilized to predict the next time velocity.

The position, mean thickness and ice concentration of each particle are evaluated with the leap-frog scheme every time step as

$$\mathbf{r}_i^{n+1} = \mathbf{r}_i^{n-1} + 2\Delta t \mathbf{u}_i^n, \tag{16}$$

$$A_i^{n+1} = A_i^{n-1} - 2\Delta t \nabla \cdot \mathbf{u}_i^n. \tag{17}$$

Typical thickness h and area S of each particle are also evaluated in a similar manner to (17).

2.2. Ice–ocean coupled model

In Section 4, we present results from experiments with an ice–ocean coupled model in order to investigate effects of density stratification of the ocean surface layer on the ice divergence.

The oceanic part of the model is represented by POM, which is a primitive equation ocean model with σ coordinates in the vertical grid (Blumberg and Mellor, 1983). The model has a square domain with a length of 500 km and a flat bottom with 1000 m depth. The horizontal grid spacing is 10 km for both x and y directions. There are 25 vertical grid cells of which 9 are concentrated within the upper 30 m in order to resolve the velocity structure of the surface boundary layer.

In the model, vertical viscosity K_M is computed by the level $2\frac{1}{2}$ turbulent closure model (Mellor and Yamada, 1982), defined by

$$K_M = qlS_M, \tag{18}$$

where l and q are turbulent length scale and turbulent kinetic energy, respectively. The turbulent exchange coefficient S_M is a function of the Richardson number, in which S_M decreases as stratification increases (Galperin et al., 1988).

As for the sea-ice component, all equations are the same as those in Section 2.1, except that the ice–water stress is modified so that ice–ocean coupling is expressed as

$$\tau_\mathrm{w} = \rho_\mathrm{w} C_{1w}|\mathbf{u} - \mathbf{u}_\mathrm{w}|(\mathbf{u}_\mathrm{w} - \mathbf{u}), \tag{19}$$

where $\mathbf{u}_w$ is current velocity of the first level (1.4 m) calculated from the ocean model. We do not include the ice–water turning angle in (19) because the surface boundary layer is represented well by the ocean model. This formula is to be used in Section 4. $\mathbf{u}_w$ at the position of the particle is interpolated from that of neighbouring grids of the ocean model by using (9). We use $C_{1w} = 5.4 \times 10^{-3}$ for numerical experiments, referring to Shirasawa and Ingram (1997), who obtained $C_w = 5.4 \times 10^{-3}$ and $\theta_w = 0°$ at a reference depth of 1 m in the Barrow Strait.

The gravity force due to ocean surface tilt $\nabla\eta$ in (1) is calculated using the geostrophic balance. In this study, we considered ocean currents at a depth of 30 m as the geostrophic current.

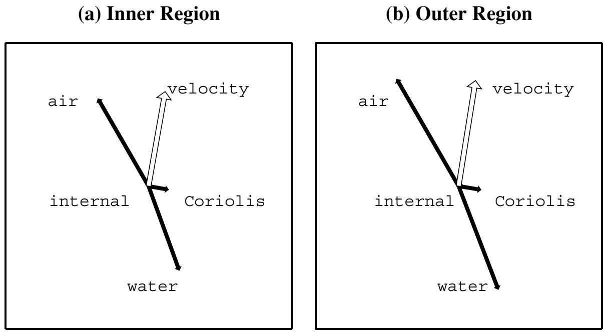

Fig. 4. Typical force balances among air drag, water drag, Coriolis force, internal forces and ice-drift vectors for 'Case A' ($A_0 = 80\%$). The forces and velocities are obtained at $r = 60$ and 120 km for (a) inner region and (b) outer region, respectively.

3. Sea ice dynamics driven by cyclonic winds

3.1. Numerical results

We carried out numerical experiments with the Lagrangian ice model described in Section 2.1 in order to clarify the mechanisms that generate sea ice divergence and variations in SIC under a low pressure system. In this section, the ocean is assumed to be at rest, and hence the gravity force due to ocean surface tilt will not be considered in (1). Since the ocean model is not coupled here, we use τ_w of (3) in this section, assuming $\theta_a = \theta_w = \frac{\pi}{6}$ as in Table 1.

First, we present results of the experiment to examine the sensitivity of SIC reduction to initial SIC (hereafter, A_0), where the radius of inner vortex R is 100 km. On the basis of the ice strength (6), we discuss results of cases with $A_0 = 80$ and 100% referred to as 'Case A' and 'Case B', respectively. The SIC distributions after 2 d are shown in Fig. 3. For 'Case A', SIC decreases intensively from the centre to $r = 60$ km and reduces to less than 90% of A_0 (Fig. 3a). This is consistent with the result of Thorndike and Colony (1982), in which the ice drift angle to the geostrophic wind is large if the ice drift velocity is sufficiently small. On the other hand, the SIC reduction near the centre of the cyclone for 'Case B' (Fig. 3b) is much smaller than that for 'Case A'. Figure 3b also shows another SIC minimum around $r = R$ (=100 km) for 'Case B'.

The mean thickness h varies in a similar manner to A based on (7), that is, sea ice becomes thinner for 'Case A' than for 'Case B' (Figures are not shown).

Figure 4 displays typical force balance among air stress, water stress, Coriolis force and internal force for 'Case A'. In both regions, the air stress, which is only external forcing, drives counter-clockwise and causes inward ice motions, while the water stress acts clockwise with outward motions. The Coriolis force accelerates the outward motion much like the water drag, although the magnitude is much smaller than that of the water drag. For 'Case A', the internal force does not act significantly. As a result, the radial velocity is in the outward direction in both regions.

When A_0 is 100% ('Case B'), the internal force is at least as strong as the Coriolis force, despite that the rest are similar to those of 'Case A' (Fig. 5). The internal force acts inward and

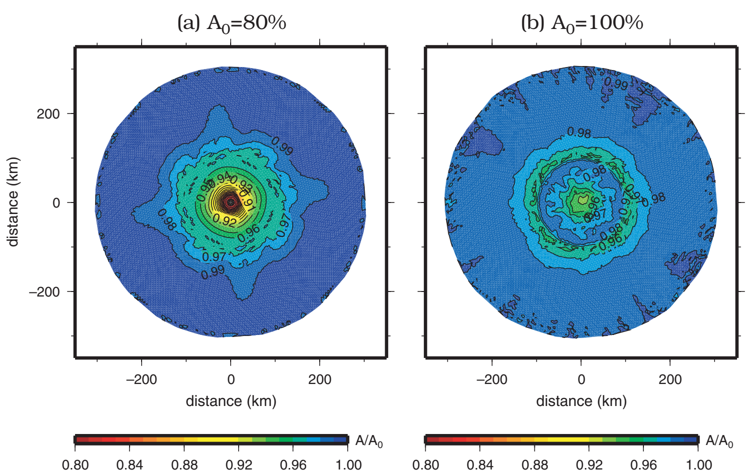

Fig. 3. SIC distributions after 2 d, normalized by initial SIC. (a) 'Case A', where $A_0 = 80\%$, and (b) 'Case B', where $A_0 = 100\%$.

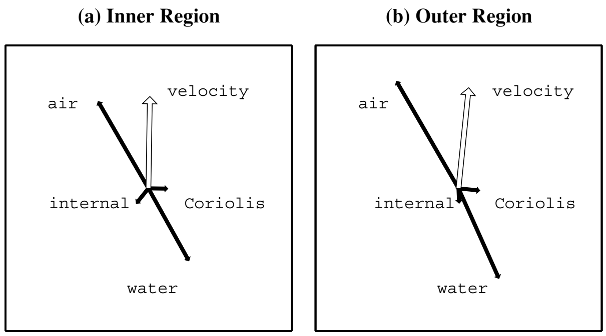

Fig. 5. Same as Fig. 4, except for the results of 'Case B' ($A_0 = 100\%$).

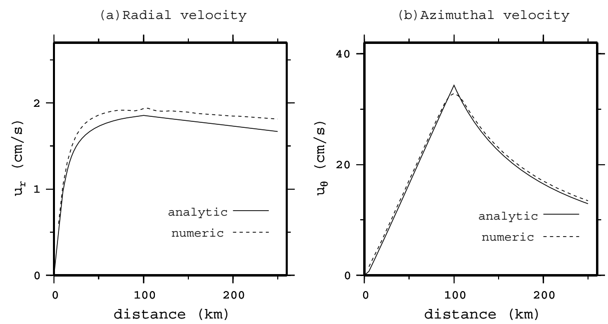

Fig. 6. (a) Radial velocities and (b) azimuthal velocities, averaged in the azimuthal direction. Solid and dashed lines denote numerical results for 'Case A' ($A_0 = 80\%$), and the analytical solutions for free drift, as in (23) and(24), respectively. The radius of the inner region is 100 km, and the wind angular velocity ω is $2.0 \times 10^{-4}\ \mathrm{s}^{-1}$.

clockwise in the inner region. As a result, $u_r \approx 0$ and trajectories of the particles are almost on a circular orbit without divergence for 'Case B', especially in the inner region, rather than drifting outward.

Figure 6 displays both velocity components for 'Case A' in terms of r, where they are averaged in the azimuthal direction. We note again that the sea ice motion is in free drift for 'Case A'. The azimuthal velocity increases linearly with distance from the centre in the inner region, but decreases inversely in the outer region (Fig. 6b); this shape is analogous to that of the geostrophic winds, that is, the Rankine vortex (Fig. 1). However, the radial velocity in the inner region increases steeply up to around $r = 20$ km, and thereafter increases gently reaching $1.9\ \mathrm{cm\,s^{-1}}$ at $r = R$. In the outer region, the radial velocity monotonously decreases with distance (Fig. 6a).

Figure 7 shows sea ice responses for 'Case A' driven by various angular velocities such as $\omega = 2.0 \times 10^{-4}$, 1.0×10^{-4} and $0.5 \times 10^{-4}\ \mathrm{s}^{-1}$. The azimuthal velocity has maximum values of 33, 17 and $8.5\ \mathrm{cm\,s^{-1}}$ for respective ω at $r = R$ (Fig. 7c). In contrast, the radial velocity is less sensitive to the variation in ω than azimuthal velocity, except in the vicinity of the centre where u_r increases with distance more rapidly as ω increases (Fig. 7b).

Figure 7a shows that intensive SIC reduction occurs near the centre, corresponding to the sharp increase of u_r as seen in Fig. 7b. Magnitude of the near-centre SIC reduction increases with ω, which has maximum values of 5.7, 4.0 and 2.1% for $\omega = 2.1 \times 10^{-4}$, 1.0×10^{-4} and $0.5 \times 10^{-4}\ \mathrm{s}^{-1}$, respectively. Away from the centre, however, it tends to be independent of ω. We will discuss in more detail the characteristic distributions of SIC and its relationship with u_r in the next section.

Next, we carried out experiments with five initial SICs (A_0 =50, 80, 95, 98 and 100%) in order to investigate effects of internal force on the SIC reduction. Figure 8 shows azimuthally averaged A/A_0, u_r and u_θ after 24 h for these five cases. The azimuthal velocities coincide with each other even though A_0 varies, and are approximately 2% of geostrophic winds in magnitude. On the other hand, there are large differences in radial velocity in terms of initial A_0, except for those of A_0 =50 and 80%; u_r becomes small for large A_0, especially in the inner region. The SIC reduction decreases markedly near the centre as A_0 increases (Fig. 8a).

Figure 9 shows numerical results for $P_0 = 25$ kPa, corresponding to five times the results in the standard case; this ice strength is frequently used for the ice drift simulations in the Arctic Ocean (e.g. Leppäranta, 2005). It is seen from Fig. 9c that the differences in u_θ among different values of A_0 become greater than those with $P_0 = 5000$ Pa, and u_r decreases more drastically. In particular, u_r becomes almost zero in the inner region for the cases with $A_0 > 0.95$.

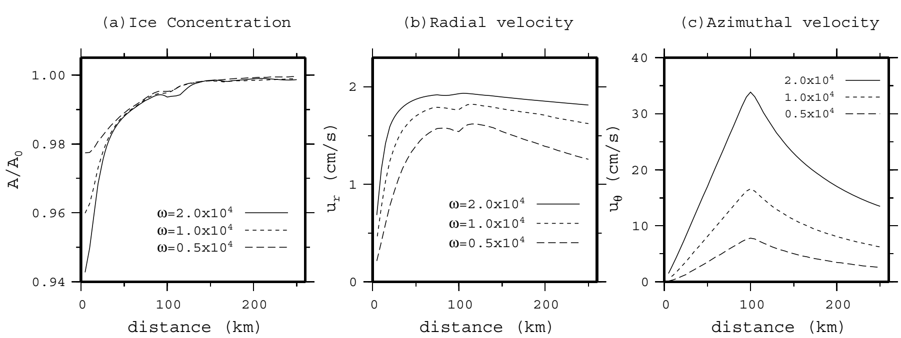

Fig. 7. (a) SICs normalized by A_0, (b) radial velocities, and (c) azimuthal velocities after 24 h for $\omega = 2.0 \times 10^{-4}\ \mathrm{s}^{-1}$ (thin line), $1.0 \times 10^{-4}\ \mathrm{s}^{-1}$ (dotted line), and $0.5 \times 10^{-4}\ \mathrm{s}^{-1}$ (dashed line). $A_0 = 80\%$ for all cases.

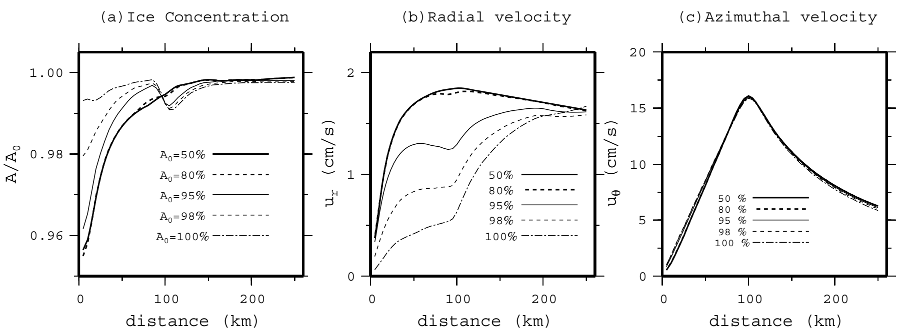

Fig. 8. (a) SICs normalized by A_0, (b) radial velocities, and (c) azimuthal velocities after 24 h for different A_0. $P_0 = 5$ kPa.

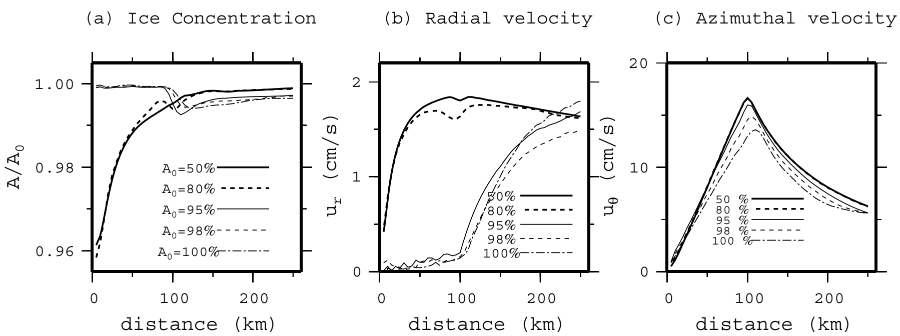

Fig. 9. Same as Fig. 8, except for $P_0 = 25$ kPa.

3.2. Analytical solutions for free drift

In this section, we describe analytical solutions for free ice drift in order to discuss the numerical results above. Assuming that the SIC tendency depends only on the divergence of ice drift, without considering thermodynamical processes, we can rewrite (7) in polar coordinates as

$$\frac{\partial A}{\partial t} = -\nabla \cdot (A\mathbf{u}) = -\frac{1}{r}\frac{\partial}{\partial r}(Au_r r), \tag{20}$$

where the condition of no azimuthal variation ($\frac{\partial}{\partial \theta} = 0$) is applied. (20) indicates that the radial velocity u_r determines the evolution of SIC. Thus, we will consider characteristics of u_r by constructing the analytical solutions.

In this subsection, the steady free-drift momentum equations are considered. As seen in the numerical solutions (e.g. Fig. 6), this assumption is valid for SIC less than 80%. It is useful to choose polar coordinates to deal with the momentum equations. Hence, we have, in non-dimensional form (cf. Leppäranta, 2005),

$$U_{\mathrm{a}}^{*2}\cos\theta_{\mathrm{a}} - (u_\theta^*\cos\theta_{\mathrm{w}} + u_r^*\sin\theta_{\mathrm{w}})|\mathbf{u}^*| - R_o h^* u_r^* = 0, \tag{21}$$

$$-U_{\mathrm{a}}^{*2}\sin\theta_{\mathrm{a}} - (u_r^*\cos\theta_{\mathrm{w}} - u_\theta^*\sin\theta_{\mathrm{w}})|\mathbf{u}^*| + R_o h^* u_\theta^* = 0, \tag{22}$$

where the non-dimensional variables are denoted by asterisks, and $R_o = \frac{\rho H f}{\rho_{\mathrm{w}} C_{\mathrm{w}} U}$ is a non-dimensional Coriolis parameter. Subscripts θ and r express radial and azimuthal components, respectively. Summary of non-dimensional numbers and scaling factors of variables is described in Appendix A.

Since the magnitude of dimensional ice speed $|\mathbf{u}|$ scales with $N_{\mathrm{a}}U_{\mathrm{a}}$, where $N_{\mathrm{a}} = (\frac{\rho_{\mathrm{a}} C_{\mathrm{a}}}{\rho_{\mathrm{w}} C_{\mathrm{w}}})^{1/2}$, we let $|\mathbf{u}^*| = U_{\mathrm{a}}^*$ here, so that $|\mathbf{u}^*|$ can be treated as a known parameter. This approximation is valid where $u_\theta^* \gg u_r^*$, although, as shown later (see Fig. 6), this gives a very good representation of the numerical solutions as a whole. These equations can then be seen as first-order linear algebraic relations of u_θ^* and u_r^*. Thus, we obtain free-drift solutions of ice motion as (cf. Thorndike and Colony, 1982)

$$u_\theta^*/U_{\mathrm{a}}^* = \frac{\cos(\theta_{\mathrm{w}} - \theta_{\mathrm{a}}) + (R_o h^*/U_{\mathrm{a}}^*)\sin\theta_{\mathrm{a}}}{(R_o h^*/U_{\mathrm{a}}^* + \sin\theta_{\mathrm{w}})^2 + \cos^2\theta_{\mathrm{w}}}, \tag{23}$$

$$u_r^*/U_{\mathrm{a}}^* = \frac{\sin(\theta_{\mathrm{w}} - \theta_{\mathrm{a}}) + (R_o h^*/U_{\mathrm{a}}^*)\cos\theta_{\mathrm{a}}}{(R_o h^*/U_{\mathrm{a}}^* + \sin\theta_{\mathrm{w}})^2 + \cos^2\theta_{\mathrm{w}}}. \tag{24}$$

We now substitute the non-dimensionalized Rankine vortex

$$U_{\mathrm{a}}^* = \begin{cases} \omega^* r^* & r^* < 1 \\ \omega^*/r^* & r^* > 1 \end{cases}$$

to (23) and (24). Figure 6 displays u_θ^* and u_r^* for $\theta_{\mathrm{a}} = \theta_{\mathrm{w}} = \pi/6$ and $\omega = 2.0\times10^{-4}$ s^{-1}. It is seen that the analytical solution is in good agreement with the numerical results in both components, although the radial component of the solution is slightly smaller than the numerical one. Figure 10a displays the solution of u_r^* for various ω^*. From the figure, u_r^* increases near the centre with increasing ω^*, whereas it assymptotically approaches to $R_o\cos\theta_{\mathrm{a}}h^*$ far away from the centre regardless of ω^*.

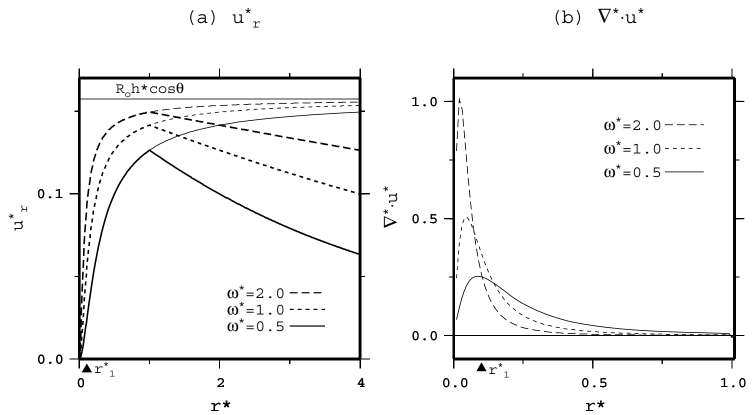

Fig. 10. Free drift solutions of (a) radial velocity and (b) ice-drift divergence, described in non-dimensional form. In the left panel, solutions for $R^* = 1$ are drawn by thick lines, and those for $R^* = 5$ by thin lines. Arrows indicate the position of r_1^* when $\omega^* = 1.0$.

Defining $\lambda \equiv \frac{U_a^*}{R_o h^*}$, (24) is rewritten as

$$u_r^*/U_a^* = \frac{\sin(\theta_w - \theta_a) + \lambda^{-1}\cos\theta_a}{\left(\lambda^{-1} + \sin\theta_w\right)^2 + \cos^2\theta_w}, \tag{25}$$

which indicates that only λ, θ_a and θ_w are responsible for the free-drift solution of u_r^*. We should note that λ indicates the strength of the water drag to the Coriolis term in the momentum balance [i.e. $\lambda = \frac{U_a^*}{R_o h^*} = O(\frac{\tau_w}{\rho H f U})$]. We may then define characteristic length scale $r_1^* \equiv R_o h^*/\omega^*$ and $r_2^* \equiv \frac{\omega^*}{R_o h^*}$ for the inner and outer regions, respectively, where the Coriolis force becomes comparable with the ice–water stress (i.e. $\lambda = 1$). This means that in the inner region, for example, the Coriolis term becomes dominant compared to the water drag (i.e. $\lambda < 1$) for $r^* < r_1^*$, while it is negligible ($\lambda > 1$) for $r^* > r_1^*$. u_r^* is expressed to the lowest order as

$$u_r^* = \begin{cases} \omega^* \cos\theta_a \frac{r^{*2}}{r_1^*} & r^* \ll r_1^* \ \ (\text{or } \lambda \ll 1), \\ R_o h^* \cos\theta_a & r^* \gg r_1^* \ \ (\text{or } \lambda^{-1} \ll 1). \end{cases} \tag{26}$$

This means that u_r increases quadratically with distance as far as $r^* \ll r_1^*$, as depicted in Fig. 10a. (26) also indicates a gradual approach of u_r^* to the assymptotical value $R_o \cos\theta_a h^*$ where $r^* \gg r_1^*$, which is also consistent with the numerical results in Section 3.1 (e.g. Fig. 6).

Similarly, in the outer region, the Coriolis term has dominant effects ($\lambda < 1$) where $r^* > r_2^*$ and much less dominant ($\lambda > 1$) where $r^* < r_2^*$. Thus, the radial velocity can be written as

$$u_r^* = \begin{cases} R_o h^* \cos\theta_a & r^* \ll r_2^* \\ \frac{\omega^* \cos\theta_a}{r_2^* r^{*2}} & r^* \gg r_2^*. \end{cases} \tag{27}$$

In the outer region, u_r^* remains constant for $r^* \ll r_2^*$, while it decreases quadratically and approaches to zero where $r^* \gg r_2^*$.

The analytical solution of ice-drift divergence, equivalent to the SIC time tendency, can be derived from (24). The solutions for various angular velocities are displayed in Fig. 10b. On the basis of λ, the ice-drift divergence can be separated again, based on r_1^*, as

$$\nabla^* \cdot \mathbf{u}^* = \begin{cases} 3\omega^* \cos\theta_a r^*/r_1^* & r^* \ll r_1^*, \\ R_o \cos\theta_a h^*/r^* & r^* \gg r_1^*, \end{cases} \tag{28}$$

in the inner region. (28) captures the characteristics of $\nabla^* \cdot \mathbf{u}^*$ shown in Fig. 10b; it increases linearly with distance where $r^* \ll r_1^*$, while it assymptotically approaches zero where $r^* \gg r_1^*$. Figure 10b and (28) show that the divergence is greatest at around $r^* = r_1^*$ for any ω^*, although its magnitude varies depending on ω^*. As a consequence, SIC decreases most rapidly around $r^* = r_1^*$, rather than at the centre, and the reduction of SIC becomes large as ω^* increases. Furthermore, the fact that the divergence depends on the angular velocity, equivalent to relative vorticity of the geostrophic wind, is in agreement with Serreze et al. (1989).

In conclusion, the ice drift divergence is characterized by λ, and a characteristic length scale r_1^* can be defined for cyclones. This implies that although we adopted $R = 100$ km in this numerical experiments, the results are also relevant for larger scale cyclones.

3.3. Steady state solution with the effect of ice interaction

The numerical results in Figs. 8 and 9 show an interesting feature, namely the radial speed gets closer to zero in the inner region when the A_0 of initial SIC increases. In this section, we clarify the momentum balance when the internal stresses are important and their role for the ice divergence. To do so, we derive a steady state solution for $u_r^* = 0$.

Assuming $u_r^* = 0$, the steady momentum balance with respect to azimuthal and radial components is given by

$$\frac{1}{r^*}\frac{\partial}{\partial r^*}(r^*\sigma_{r\theta}^*) + \cos\theta\left(U_a^{*2} - u_\theta^{*2}\right) = 0, \tag{29}$$

$$\frac{1}{r^*}\frac{\partial}{\partial r^*}(r^*\sigma_{rr}^*) - \sin\theta\left(U_a^{*2} - u_\theta^{*2}\right) + R_o h^* u_\theta^* = 0, \tag{30}$$

where $\theta = \theta_a = \theta_w$. In (29) and (30), we replaced $|\mathbf{u}^*|$ with u_θ^*, because $u_r^* = 0$. (29) indicates that in azimuthal momentum balance, internal shear stress yields a decrease of u_θ^* relative to free drift velocity U_a^*. In the radial component (30), the Coriolis force is balanced by compressive internal stress force due to ice strength. The difference between air stress and water stress, with turning angle θ, also contributes to the radial momentum balance. Balance of forces in the numerical experiments (Fig. 5a) agrees with those described by (29) and (30).

We should note that in the experiments, sea ice behaviour follows a plastic rheology rather than a linear viscous rheology, because the strain rate whose magnitude is $O(10^{-6})\,\mathrm{s}^{-1}$ is substantially larger than maximum creep rate ($\Delta_0 = 2 \times 10^{-9}\,\mathrm{s}^{-1}$). Therefore, we have $\sigma_{rr}^* = -P^*/2$ and $\sigma_{r\theta}^* = \frac{P^*}{2e}\mathrm{sgn}(\dot{\varepsilon}_{r\theta}^*)$ (see Appendix B). Since $\dot{\varepsilon}_{r\theta}^* = \frac{\partial u_\theta^*}{\partial r^*} - \frac{u_\theta^*}{r^*}$, $\dot{\varepsilon}_{r\theta}^*$ is zero for a solid rotation in the inner region of the Rankine vortex, while it is $-\frac{2u_\theta^*}{r^*}$ for an irrotational flow in the outer region. Therefore, $\dot{\varepsilon}_{r\theta}^*$ tends to be negative when u_θ^* is modified by friction. For example, since $\frac{\partial u_\theta^*}{\partial r^*} = 0$ at the position of maximum velocity (at about $r^* = 1$), we have $\dot{\varepsilon}_{r\theta}^* \approx -\frac{u_\theta^*}{r^*} < 0$ around there. Considering the arguments above, we finally obtain $\sigma_{r\theta}^* = -\frac{P^*}{2e}$. Eliminating the internal stress terms from (29) and (30), this leads to

$$u_\theta^*/U_a^* = \sqrt{1 + \frac{1}{4\lambda^2(e\cos\theta + \sin\theta)}} - \frac{1}{2\lambda(e\cos\theta + \sin\theta)}. \tag{31}$$

In the region where $r^* \gg r_1^*$ (or $\lambda^{-1} \ll 1$), (31) may be reduced to

$$u_\theta^*/U_a^* \approx 1 - \frac{1}{2\lambda(e\cos\theta + \sin\theta)}. \tag{32}$$

Therefore, a steady state with $u_r^* = 0$ can be achieved if the azimuthal velocity is decelerated by $O(\lambda^{-1})$ relative to U_a^* due to the shear stress. Since λ^{-1} [$= O(R_o)$] is about 0.1 for the parameters in Table 1 and $U = 0.2$ ms^{-1}, the steady solution predicts that the azimuthal velocity is decreased by 1–2 cm s^{-1}, consistent with the numerical results in Fig. 9. At the same time, the ice rheology yields $\frac{\partial}{\partial r^*}(r^*\sigma_{rr}^*) = e\frac{\partial}{\partial r^*}(r^*\sigma_{r\theta}^*) < 0$, and hence the compressive stress can balance with the Coriolis force in (30) and prevent sea ice from drifting outward. This is also consistent with the balance of forces in Fig. 5.

We may also interpret the numerical results as follows. First, $u_r^* \approx 0$ occurs around $r^* = 1$ because u_θ^* is decelerated substantially due to the above process, where u_θ^* is the maximum. Once $u_r^* = 0$ is achieved around $r^* = 1$, u_r^* for $r^* < 1$ is also blocked and converges to zero, opposing to the sea-ice tendency to drift outward under cyclonic forcing. Outside $r^* = 1$, however, there are no locations where u_r^* is forced to be zero, and therefore, sea ice drifts outward even though SIC is large.

If we scale the magnitude of internal stress X and R_o (see Appendix A) with the parameter values in Table 1, as well as with $U = 0.2$ ms^{-1}, $L = R = 100$ km and $P_0 = 25\,000$ Pa, then we have $X \approx 1$ and $R_o \approx 0.1$. Since $P^* = O(10^{-1})$ for $A = 0.9$ (see eq. 6), the internal stress and Coriolis force are able to balance with each other up to the value of A. If A becomes smaller than 0.9, P^* also decreases quickly, thus the internal stress terms no longer contribute to the momentum balance; u_r^* must be considered to be balanced with the Coriolis force in this case, and therefore the free-drift solution should become relevant. This is consistent with the numerical results shown in Fig. 10b, in which $u_r^* \approx 0$ occurs for $A > 0.95$, while u_r^* exhibits the free-drift solution for $A < 0.8$.

4. Effects of oceanic stratification on ice divergence

In this section, we will examine how the Ekman flow near the surface, whose structure varies depending on the oceanic stratification, affects the ice divergence responding to cyclonic winds. This subject is associated with how θ_w in (24) is determined through ice–ocean interaction processes. To do so, we used the ice–ocean coupled model with vertically fine resolution, which can reproduce the Ekman flow within the surface layer. In this section the water stress τ_w is in the form of (19).

The upper part of the Arctic Ocean is frequently characterized by a well-mixed surface layer, of which thickness varies sensitively with season and location. For example, in winter, the strong convection by freezing penetrates the halocline formed during summer and makes the mixed layer quite deeper; it reaches 30–50 m in strongly stratified seas by large fresh water input due to river runoff (e.g. Canada Basin or Siberian Shelf), while it could exceed 100 m in relatively weakly stratified regions such as Nansen Basin (Rudels et al., 1996). In summer, ice melting and high river runoff can generate strong stratification immediately beneath the surface and reduce the mixed layer depth to less than 10 m (Rudels et al., 1996).

To date, most ice models, as well as ice–ocean coupled models, have assumed temporally and spatially constant θ_w. However, the Ekman flow structure may vary significantly as stratification changes. Here, we performed numerical experiments without assuming θ_w a priori to provide insights into the SIC reduction in the presence of a stratified surface layer.

In this experiments, we set stratification to depend on salinity only (Fig. 11). Two kinds of salinity profiles were used. One has a profile that increases with depth linearly from the surface to a depth of 82 m, and retains its value at deeper depths. Seven cases were considered, where the salinity difference within the surface layer, ΔS, varies from 0 to 2.5 psu, which is equivalent to a density difference of 0–2.0 kg m^{-3}. The other profile is expressed by a hyperbolic function (dashed line in Fig. 11), which models a well-mixed surface layer and a halocline at 30–60 m depth. Temperature is fixed to 0 °C at any level and SIC is initially 80% for all cases.

Figure 12 shows SIC distributions for $\Delta S = 0.1$ and 2.5 psu after 2 d. When $\Delta S = 0.1$ psu, a weakly stratified case, the SIC reduction is 7–8% at most mainly in the inner region, while for

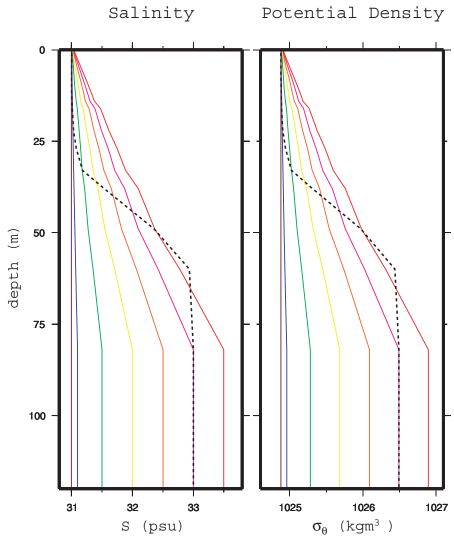

Fig. 11. Model vertical profiles of salinity (left-hand side) and potential density (right-hand side) in the ocean upper layer. Potential temperature is 0 °C at any depth. Solid colour lines denote the continuously stratified cases (seven cases). Dashed line denotes the well-mixed surface layer case.

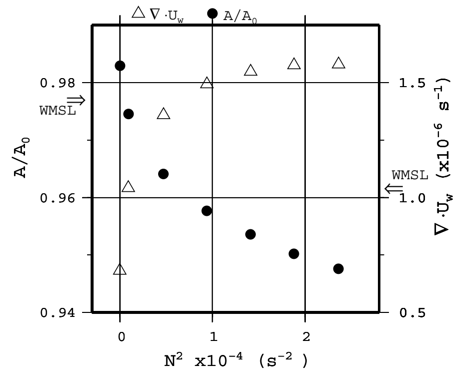

Fig. 13. SICs (filled circle) normalized by A_0 after 24 h, and ocean surface divergence at a depth of 1.4 m (triangle). Each value represents the average over the inner region (r < 100 km). Arrows indicate each value for the well-mixed surface layer (WMSL) (dashed line in Fig. 11). N is the Brunt-Väisälä frequency.

$\Delta S = 2.5$ psu, SIC reduces by more than 20% near the centre. Figure 13 shows the relationship between the Brunt–Väisälä frequency N^2 and mean A/A_0 in the inner region after 24 h, in which A/A_0 has an inverse relationship to N^2, meaning that the reduction in SIC becomes large as the near-surface stratification is strengthened (see also Fig. 12).

Figure 13 also shows that the near-surface divergence increases with N^2. Therefore, when the density gradient is sharp within the surface layer, the strengthened divergent Ekman flow promotes the ice divergence, resulting in the SIC reduction.

Top panels of Fig. 14 show the water surface divergence for $\Delta S = 2.5$ and 0.1 psu. Clearly, the surface divergence in the inner region (i.e. r< 100 km) is much greater for $\Delta S = 2.5$ psu than that for $\Delta S = 0.1$ psu. Vertical profiles of water divergence averaged in the inner region are depicted in Fig. 15. Except for the case of $\Delta S = 0$ psu, the divergent flow is limited to a thin layer near the surface, whose thickness decreases as ΔS becomes large.

Figure 14 also displays vertical structures of upwelling in the surface layer for both cases of ΔS. It can be seen that strong upwelling occurs beneath a depth of 20 m irrespective of ΔS. The upwelling reaches its maximum at around 30 and 15 m in depth for $\Delta S = 0.1$ and 2.5 psu, respectively, where the divergence is zero in Fig. 15. The upwelling gradually decreases from the depth of maximum upwelling to the surface. Since the depth of maximum upwelling may be considered to be the base of the Ekman layer, the Ekman-layer thicknesses D_e are estimated to be 30 and 15 m for the cases of $\Delta S = 0.1$ and 2.5 psu, respectively.

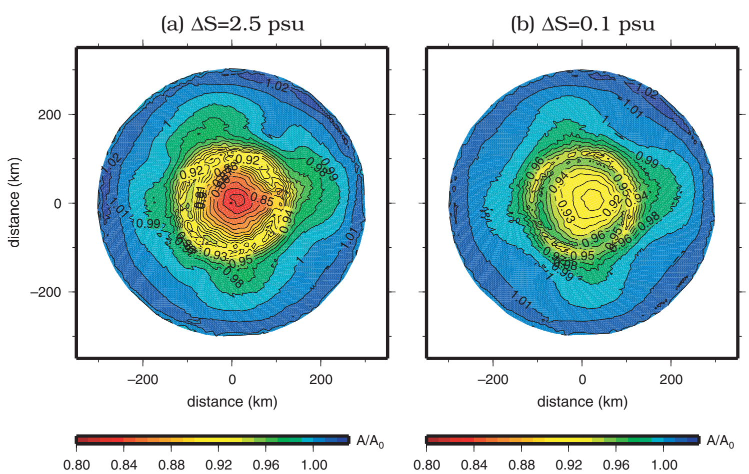

Fig. 12. SIC distributions after 2 d, normalized by A_0, for (a) $\Delta S = 2.5$ psu and (b) $\Delta S = 0.1$ psu within 82 m in the surface layer. The initial SIC is 80% for both cases.

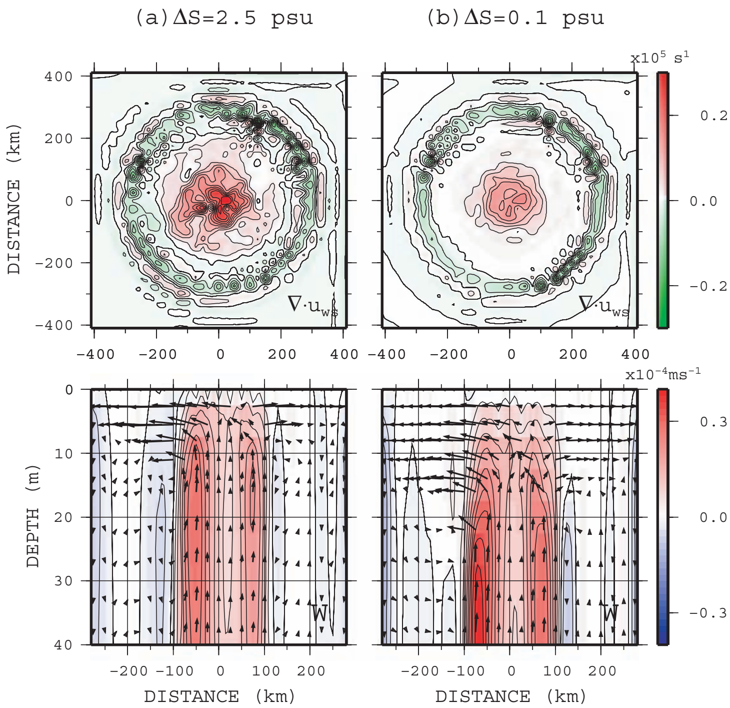

Fig. 14. Ocean surface divergence at 1.4 m depth (top) and zonal sections of upwelling in the ocean surface layer (bottom) for (a) $\Delta S = 2.5$ psu and (b) $\Delta S = 0.1$ psu.

The thickness of the Ekman layer can also be estimated by

$$\delta_e = \sqrt{\frac{2K_M}{f}}, \tag{33}$$

where K_M and f denote the vertical viscosity and Coriolis parameter, respectively. In this model, K_M is evaluated based on the Richardson number, as in (18). The estimates of δ_e from (33) and K_M for various values of ΔS are shown in Table 2. As expected, K_M, and hence δ_e, tend to be smaller as stratification becomes stronger (Mellor and Yamada, 1982; Galperin et al., 1988). Since δ_e is an e-folding scale of the Ekman layer thickness, if we take $D_e \simeq 2\delta_e$, both thickness estimations correspond with each other.

Since the total horizontal transport within the surface Ekman layer must be the same regardless of δ_e, the divergent flows immediately beneath the surface should become larger as the Ekman layer becomes thinner. Thus, as the stratification becomes stronger in the surface layer, the enhanced divergent flows drive sea ice further outward, and consequently promote the sea ice divergence. Therefore, it is concluded that the stronger oceanic stratification generates larger ice divergence and SIC reduction, accompanied by the Ekman layer thinning.

In the second experiment, in which a well-mixed surface layer is situated above a halocline below 30 m, SIC reduction and Ekman divergence are quite similar to those of the case with $\Delta S = 0.1$ psu (Fig. 13). The vertical structure of water divergence coincides with that of $\Delta S = 0.1$ psu as well (Fig. 15). It is interesting to see that D_e for $\Delta S = 0.1$ psu is 30 m, which is the same as the thickness of the well-mixed surface layer in the halocline experiment. Therefore, if a well-mixed surface layer is present, the effects of stratification may be evaluated in terms of the depth of the halocline.

Next, we estimate the ice–water turning angle θ_{w} based on the numerical results. In order to calculate this, we first estimated the angles of sea ice drift and surface water flow from the geostrophic currents, that is, ϕ_i and ϕ_{w}, respectively (Fig. 16). Since $\nabla \cdot \mathbf{u} = (\frac{1}{r} + \frac{\partial}{\partial r})u_r$ and $\nabla \times \mathbf{u} = (\frac{1}{r} + \frac{\partial}{\partial r})u_\theta$ in polar coordinates, ϕ_i and ϕ_{w} may be calculated, respectively, from

$$\tan\phi \approx \nabla \cdot \mathbf{u}/\nabla \times \mathbf{u}. \tag{34}$$

We then evaluated θ_{w} geometrically using ϕ_i and ϕ_{w} as in Fig. 16.

Figure 17 shows that θ_{w} varies sensitively with N^2 from 12° to 34°. Since $|\mathbf{u}_{\mathrm{i}}|$ is approximately 20 cm s^{-1} regardless of N^2 (figure not shown), the variation in θ_{w} is caused mainly by changes in $|\mathbf{u}_{\mathrm{w}}|$; it varies from 5.5 to 9.3 cm s^{-1} (Fig. 17) associated with the increase of Ekman divergence as stratification increases. The increase of ϕ_{w} for $N^2 < 0.5$ also contributes to the sensitivity of θ_{w} to stratification.

Most studies on Arctic sea ice have used $\theta_{\mathrm{w}} = 25°$ as a typical angle (Leppäranta, 2005), which is a result of AIDJEX field studies in the Beaufort Sea (McPhee, 1982). However, as seen from the numerical results, the ice–water turning angle with respect to geostrophic currents depends greatly on the stratification. Therefore, θ_{w} needs to be chosen appropriately for numerical models and data analysis. In summer, the fresh water input from melting ice or river runoff often creates strong salinity stratification of $\Delta S = 1.0$ psu within a 30 m-deep surface layer, giving $N^2 = 2.5 \times 10^{-4}$ s^{-2} (Rudels et al., 1991). In this case, θ_{w} is as large as

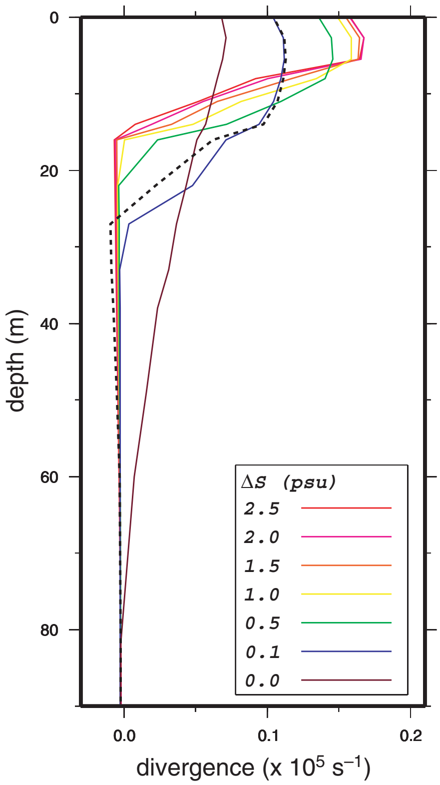

Fig. 15. Vertical profiles of horizontal divergence in the surface layer, which are averaged in the inner region at each depth. Dashed line is that for the halocline model in Fig. 11.

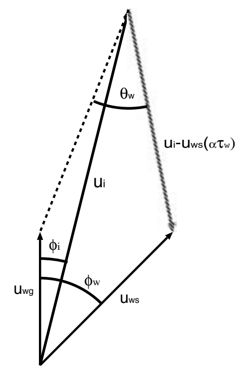

Fig. 16. Schematic figure for the estimate of water turning angle θ_{w}. ϕ_i and ϕ_{w} are direction angles of ice and surface water velocities from geostrophic currents, respectively, and they are evaluated from $\phi = \tan^{-1}(\nabla \cdot \mathbf{u}/\nabla \times \mathbf{u})$. $\mathbf{u}_{\mathrm{ws}}$, $\mathbf{u}_{\mathrm{wg}}$ and $\mathbf{u}_{\mathrm{i}}$ indicate the ocean surface current, the geostrophic currents and the ice drift vector, respectively. $|\mathbf{u}_{\mathrm{wg}}| = |\mathbf{u}_{\mathrm{ws}}|$ is assumed for the estimate of θ_{w}.

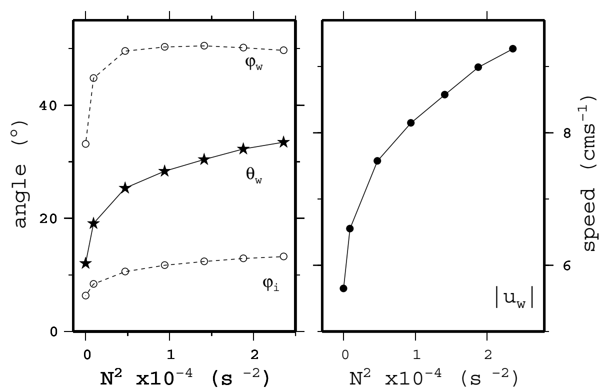

Fig. 17. (Left-hand panel) Mean values for water turning angle θ_{w}, ice drift angle ϕ_i, and surface current angle ϕ_{w} from the geostrophic currents. (Right-hand panel) Magnitudes of surface current at a depth of 1.4 m. All variables are averaged over $r < 100$ km.

Table 2. The relation between Brunt-Väisälä frequency N^2 and Ekman layer thickness δ_e. The vertical viscosity K_M is evaluated by the turbulent closure model at every time step and averaged over 24 h

Case	ΔS (psu)	N^2 $\times 10^{-5}$ (s^{-2})	K_M $\times 10^{-3}$ ($m^2 s^{-1}$)	δ_e (m)
1	2.5	23.6	6.0	10.9
2	2.0	18.8	6.4	11.3
3	1.5	14.0	6.6	11.5
4	1.0	9.4	6.8	11.7
5	0.5	4.7	7.2	12.0
6	0.1	0.9	9.7	14.0
7	0.0	0.0	22.5	21.2

30°–35°. In winter, when the upper layer is more homogeneous, θ_{w} is likely to be 20° at most. Therefore, the difference in the surface stratification between winter and summer can be large enough to change the ice divergence by a factor of two.

5. Concluding remarks

The main goal of this study was to understand dynamics of ice divergence under a low pressure system, and yield insight on seasonal changes of SIC variation. We performed analytical and numerical experiments of sea-ice motion in a circle ice region, driven by geostrophic winds of the Rankine combined vortex. The numerical experiments were performed by using the SPH method. The results are summarized as follows.

First, we discussed characteristics of SIC reduction due to cyclonic winds in free drift cases ($A_0 < 80\%$ in the model). We have found a characteristic length scale, r_1^*, based on the influence of the Coriolis term. Near the centre where $r^* < r_1^*$, the outward radial velocity, which causes the divergence and SIC reduction, quadratically increases with distance. In contrast, where $r^* > r_1^*$, the increase of u_r^* gradually becomes gentle, and consequently, ice-drift divergence assymptotically approaches a constant value. As a result, SIC reduction is largest at about $r^* = r_1^*$.

Second, the influences of internal stress on ice motion are also examined. According to the numerical results, SIC reduction decreases drastically with increasing A_0, especially in the inner region. We have obtained a steady state solution with a zero radial velocity, where the radial and azimuthal momentum equations are coupled through the Hibler's plastic rheology. We concluded that the blocking of outward velocity, and consequently the decrease of ice divergence, is due to a balance between the compressive stress and the Coriolis force within the inner region, which is coupled with deceleration of the azimuthal velocity due to shear stress.

Finally, we numerically examined the effects of ocean surface stratification on the ice divergence under a low pressure system. We found that the ice divergence increases as the ocean stratification is strengthened. The estimated ice–water turning angle varies from $\theta_w = 12°$ to $34°$. The enhanced divergence for the strongly stratified layer is explained by thinning of the Ekman layer as the vertical viscosity decreases. The difference in stratification between summer and winter can be large enough to change ice divergence by a factor of 2.

The ice divergence leads to enhanced heat absorption and ice melting in the resultant open water in summer, which strengthens the surface stratification and reduces ice concentrations. These processes promote ice divergence further and therefore generate broader open water areas as studied in this paper. In addition, the upward heat flux from the open water fraction makes the atmosphere unstable and θ_a tends to be smaller (e.g. Thorndike and Colony, 1982; Leppäranta, 2005), also accerelating the ice divergence. These interactions among atmosphere–ice–ocean are likely to give rise to positive feedback effects for the decay of ice, and should contribute to the summer regression of the Arctic ice associated with persistent low pressure systems (e.g. Serreze et al., 2003). The complicated interaction processes merit further studies in the future.

6. Acknowledgments

We thank Prof. M. Leppäranta of Helsinki University, Prof. M. Ikeda and Dr. T. Toyota of Hokkaido University for their valuable comments and advice on this study. We also thank Dr. Lindsay of University of Washington for his advice to development of the Lagrangian ice model. The manuscript was improved greatly by comments from anonymous reviewers. English was proofread by Tak Ikeda. The numerical experiments were performed on Pan-Okhotsk information System of ILTS, Hokkaido University.

7. Appendix A: Derivation of non-dimensional momentum equations

For a quantitative consideration, the momentum equation can be rewritten by using the following dimensionless quantities:

$$
\begin{aligned}
r^* &= \frac{r}{L},\\
t^* &= \frac{U}{L}t,\\
(u_\theta^*, u_r^*) &= (u_\theta, u_r)/U,\\
|\mathbf{u}^*| &= \frac{|\mathbf{u}|}{U},\\
U_a^* &= \frac{N_a}{U}U_a,\\
h^* &= \frac{h}{H},\\
\omega^* &= \frac{N_a L}{U}\omega,\\
\sigma^* &= \frac{\sigma}{P_0 H},
\end{aligned}
$$

where $N_a (= \sqrt{\frac{\rho_a C_a}{\rho_w C_w}})$ is a Nansen number. By scaling each term based on the magnitude of water drag $\rho_w C_w U^2$, the azimuthal component of the momentum equation is given by

$$
\begin{aligned}
\frac{\rho H}{\rho_w C_w L} h^* \frac{\partial u_\theta^*}{\partial t^*} + \frac{\rho H}{\rho_w C_w L} h^* \mathbf{u}^* \cdot \nabla^* u_\theta^* &= U_a^{*2} \cos\theta_a \\
&- (u_\theta^* \cos\theta_w + u_r^* \sin\theta_w)|\mathbf{u}^*| - \frac{\rho H f}{\rho_w C_w U} h^* u_r^* \\
&+ \frac{P_0 H}{\rho_w C_w U^2 L} \nabla^* \cdot \sigma^*,
\end{aligned}
\tag{A.1}
$$

where subscripts θ and r show radial and azimuthal components, respectively. Further, introducing an inertial time scale $T_I \equiv \frac{\rho H}{\rho_w C_w U}$ and non-dimensional parameters such as ice Rossby number $R_o \equiv \frac{\rho H f}{\rho_w C_w U} = T_I f$ and friction number $X \equiv \frac{P_0 H}{\rho_w C_w L U^2}$ (cf. Leppäranta, 2005), (A.1) can be written as

$$
\begin{aligned}
\frac{T_I}{T}\left(h^* \frac{\partial u_\theta^*}{\partial t^*} + h^* \mathbf{u}^* \cdot \nabla u_\theta^*\right) &= U_a^{*2} \cos\theta_a \\
&- (u_\theta^* \cos\theta_w + u_r^* \sin\theta_w)|\mathbf{u}^*| - R_o h^* u_r^* \\
&+ X(\nabla^* \cdot \sigma^*)_\theta,
\end{aligned}
\tag{A.2}
$$

where an advective time scale is defined to be $T \equiv U/L$. The radial component can also be derived in the same way.

Note that T_I is short enough to be ignored in comparison with advective time scale $T = O(10^6)s$. For example, when $U = 0.1\ \mathrm{ms}^{-1}$ and $H = 1$ m, the magnitude of inertial time scale T_I is $O(10^3)\ s$. Hence, we can simply consider the momentum balance only by the terms on the right-hand side of (A.2).

8. Appendix B: Internal stress tensor in polar coordinates

The internal stress needs to be expressed by a strain rate explicitly for an analytical discussion. Assuming θ-invariant motions (i.e. $\frac{\partial}{\partial\theta} = 0$) and the polar coordinate system, internal stress is

$$
\sigma = \frac{P}{2}\left(\frac{\dot{\varepsilon}_I}{\Delta} - 1\right)\mathbf{I} + \frac{P}{2e^2\Delta}\dot{\varepsilon}',
$$

where

$$\dot{\varepsilon} = \begin{bmatrix} \frac{\partial u_r}{\partial r} & \frac{1}{2}\left(\frac{\partial u_\theta}{\partial r} - \frac{u_\theta}{r}\right) \\ \frac{1}{2}\left(\frac{\partial u_\theta}{\partial r} - \frac{u_\theta}{r}\right) & \frac{u_r}{r} \end{bmatrix},$$

$$\dot{\varepsilon}' = \dot{\varepsilon} - \frac{1}{2}\mathrm{tr}\dot{\varepsilon}\mathbf{I},$$

$$\Delta = \sqrt{\dot{\varepsilon}_I + \frac{\dot{\varepsilon}_{II}}{e^2}},$$

$$\dot{\varepsilon}_I = \mathrm{tr}\dot{\varepsilon},$$

$$\dot{\varepsilon}_{II} = \sqrt{\mathrm{tr}\dot{\varepsilon} - 4\det\dot{\varepsilon}}.$$

If the radial strain rate is small enough to be neglected ($u_r \to 0$), σ_{rr} and $\sigma_{r\theta}$ result in

$$\sigma_{rr} = -P/2,$$

$$\sigma_{r\theta} = \frac{P}{2e}\mathrm{sgn}(\dot{\varepsilon}_{r\theta}) = \frac{P}{2e}\mathrm{sgn}\left(\frac{\partial u_\theta}{\partial r} - \frac{u_\theta}{r}\right).$$

References

Blumberg, A. F. and Mellor, G. L. 1983. Diagnostic and prognostic numerical circulation studies of the South-Atlantic Bight. *J. Geophys. Res.* **77**(NC8), 4579–4592.

Cavalieri, D. J., Gloersen, P., Parkinson, C. L., Comiso, J. C. and Zwally, H. J. 1997. Observed hemispheric asymmetry in global sea ice changes. *Science* **278**, 1104–1106.

Comiso, J. C. 2006. Abrupt decline in the Arctic winter sea ice cover. *Geophys. Res. Lett.* **33**, L18504.

Galperin, B., Kantha, L. H., Hassid, S. and Rosati, A. 1988. A quasi-equilibrium turbulent energy model for geophysical flows. *J. Atmos. Sci.* **45**, 55–62.

Gutfraind, R. and Savage, S. B. 1997. Smoothed particle hydrodynamics for the simulation of broken-ice fields: Mohr-Coulomb-type rheology and frictional boundary conditions. *J. Comput. Phys.* **134**, 203–215.

James, R. W. 1950. On the theory of large-scale vortex motion in the atmosphere. *Q. J. Roy. Met. Soc.* **67**, 255–276.

Johannessen, O. M., Miles, M. and Bjørgo, E. 1995. The Arctic's shrinking sea ice. *Nature* **376**, 126–127.

Haapala, J., Lönnroth, N. and Stössel, A. 2005. A numerical study of open water formation in sea ice. *J. Geophys. Res.* **110**(C9), C09011.1–C09011.17.

Hibler, W. D. III 1979. A dynamic thermodynamic sea ice model. *J. Phys. Oceanogr.* **9**, 815–846.

Leppäranta, M. 2005. *The Drift of Sea Ice.* Springer-Verlag, Berlin and New York, 266 pp.

Lindsay, R. W. and Stern, H. L. 2004. A new Lagrangian model of Arctic sea ice. *J. Phys. Oceanogr.* **34**, 272–283.

Maslanik, J. A., Serreze, M. C. and Barry, R. G. 1996. Recent decreases in Arctic summer ice cover and linkages to atmospheric circulation anomalies. *Geophys. Res. Lett.* **23**(No. 13), 1677–1680.

Maykut, G. A. and Perovich, D. K. 1987. The role of shortwave radiation in the summer decay of a sea ice cover. *J. Geophys. Res.* **92**, 7032–7044.

McPhee, M. G. 1982. Sea Ice Drag Laws and Simple Boundary Layer Concepts, Including Application to Rapid Melting (Report 82-4). US Army Cold Regions Research and Engineering Laboratory, Hanover, NH.

Mellor, G. L. and Yamada, T. 1982. Development of a turbulence closure model for geophysical fluid problems. *Rev. Geophys. Space Phys.* **20**(4), 851–875.

Nghiem, S. V., Rigor, I. G., Perovich, D. K., Clemente-Colón, P., Weatherly, J. W., and co-authors. 2007. Rapid reduction of Arctic perennial sea ice. *Geophys. Res. Lett.* **34**, L19504.

Ohshima, K. I. and Nihashi, S. 2005. A simplified ice-ocean coupled model for the Antarctica ice melt season. *J. Phys. Oceanogr.* **35**(2), 188–201.

Rudels, B., Larsson, A.-M. and Sehlstedt, P.-I. 1991. Stratification and water mass formation in the Arctic Ocean: some implications for the nutrient distribution. *Polar Res.* **10**(1), 19–31.

Rudels, B., Anderson, L. G. and Jones, E. P. 1996. Formation and evolution of the surface mixed layer and halocline of the Arctic Ocean. *J. Geophys. Res.* **101**(c4), 8807–8821.

Shapiro, M. A., Fedor, L. S. and Hampel, T. 1987. Research aircraft measurements of a polar low over Norwegian Sea. *Tellus,* **39A**, 272–306.

Serreze, M. C., Barry, R. G. and McLaren, A. S. 1989. Seasonal variations in sea ice motion and effects on sea ice concentration in the Canada Basin. *J. Geophys. Res.* **94**(8), 10955–10970.

Serreze, M. C., Maslanik, J. A., Scambos, T. A., Fetterer, F., Stroeve, J., and co-authors. 2003. A record minimum arctic sea ice extent and area in 2002. *Geophys. Res. Lett.* **30**(3), 1110 .

Shirasawa, K. and Ingram, R. G. 1997. Currents and turbulent fluxes under the first-year sea ice in Resolute Passage, Northwest Territories, Canada. *J. Mar. Syst.* **11**, 21–32.

Steel, M. and Boyd, T. 1998. Retreat of the cold halocline layer in the Arctic Ocean. *J. Geophys. Res.* **103**(c5), 10419–10435.

Stroeve, J., Holland, M. M., Meier, W., Scambos, T. and Serreze, M. 2007. Arctic sea ice decline: faster than forecast. *Geophys. Res. Lett.* **34**, L09501.

Thorndike, A. S. and Colony, R. 1982. Sea ice motion in response to geostrophic winds. *J. Geophys. Res.* **87**(c8), 5845–5852.